

# Direct observation of spin-quadrupolar excitations in $\text{Sr}_2\text{CoGe}_2\text{O}_7$ by high field ESR

Mitsuru Akaki,<sup>1,\*</sup> Daichi Yoshizawa,<sup>1</sup> Akira Okutani,<sup>1</sup> Takanori Kida,<sup>1</sup> Judit Romhányi,<sup>2</sup> Karlo Penc,<sup>3,4</sup> and Masayuki Hagiwara<sup>1</sup>

<sup>1</sup>Center for Advanced High Magnetic Field Science, Graduate School of Science, Osaka University, Toyonaka, Osaka 560-0043, Japan

<sup>2</sup>Okinawa Institute of Science and Technology Graduate University, Onna-son, Okinawa 904-0395, Japan

<sup>3</sup>Institute for Solid State Physics and Optics, Wigner Research Centre for Physics, Hungarian Academy of Sciences, H-1525 Budapest, P.O.B. 49, Hungary

<sup>4</sup>MTA-BME Lendület Magneto-optical Spectroscopy Research Group, 1111 Budapest, Hungary

(Dated: July 17, 2022)

Exotic spin-multipolar ordering in spin transition metal insulators has so far eluded unambiguous experimental observation. A less studied, but perhaps more feasible fingerprint of multipole character emerges in the excitation spectrum in the form of quadrupolar transitions. Such multipolar excitations are desirable as they can be manipulated with the use of light or electric field and can be captured by means of conventional experimental techniques. Here we study single crystals of multiferroic  $\text{Sr}_2\text{CoGe}_2\text{O}_7$ , and show that due to its nearly isotropic nature a purely quadrupolar bimagnon mode appears in the electron spin resonance (ESR) spectra. This non-magnetic spin-excitation couples to the electric field of the light and becomes observable for a specific experimental configuration, in full agreement with a theoretical analysis of the selection rules.

## I. INTRODUCTION

Multipole moments formed by neighboring spins can simultaneously break time-reversal and spatial inversion symmetries, allowing for magneto-electric coupling and the mutual control of magnetization by electric and polarization by magnetic fields, providing new multiferroic materials for future technologies [1–4]. Well known examples are vector spin chirality and exchange striction driven electricity [5–7], both involving more than one spin. In the vector spin chirality mechanism, the non-collinearity of the neighboring magnetic moments may induce electric polarization, while in the exchange striction case the charged magnetic ions move to optimize the Heisenberg exchange energy between the neighbours with parallel and antiparallel magnetic moments.

Remarkably, in  $\text{\AA}$ kermanites – where  $\text{CoO}_4$  tetrahedra form diagonal square lattices, alternating with interven-

ing layers of alkaline earth metal ions along the  $c$ -axis [Fig. 1] – the electric polarization is not induced by correlations between neighbouring spins, but is also present in the paramagnetic phase [8]. These compounds represent an exceptional family of magneto-electric materials, in which the finite (on-site) polarization emerges on the account of relativistic metal-ligand hybridization [9]. For this mechanism at least two conditions have to meet: The transition metal ion has to carry a spin larger than  $1/2$  and the inversion symmetry on this site needs to be broken. The spin- $3/2$  magnetic moment of  $\text{Co}^{2+}$  allows for higher order multipole operators, such as the required quadrupole moment related to the emerging on-site polarization. Furthermore, the lack of inversion symmetry at Co sites permits magneto-electric coupling already for a single ion. The metal-ligand hybridization is believed to act in  $\text{Ba}_2\text{CoGe}_2\text{O}_7$  [10, 11],  $\text{Sr}_2\text{CoSi}_2\text{O}_7$  [8], and  $\text{Ca}_2\text{CoSi}_2\text{O}_7$  [12, 13]. This mechanism is considered to be responsible for the dynamical properties of these materials, allowing for a coupling of spin-states to the oscillating electric field component of the light.

$\text{\AA}$ kermanites are usually characterized by large easy-plane magnetic anisotropy and small exchange interaction. As a consequence the spin dipole and quadrupole degrees of freedom become mixed and it is challenging to untangle the different types of multipolar fluctuations in the excitation spectra. This is well exemplified in the THz absorption spectra by the observation of the ‘electromagnon’ in  $\text{Ba}_2\text{CoGe}_2\text{O}_7$ , an electrically active magnetic excitation having both dipolar and quadrupolar character [14–16].

Here we report on the properties of  $\text{Sr}_2\text{CoGe}_2\text{O}_7$ , a member of the  $\text{\AA}$ kermanite family with almost isotropic magnetization properties. When the magnetic anisotropies are small or absent, the different multipolar degrees of freedom do not mix, reflecting the higher symmetry of the system. Using electron spin reso-

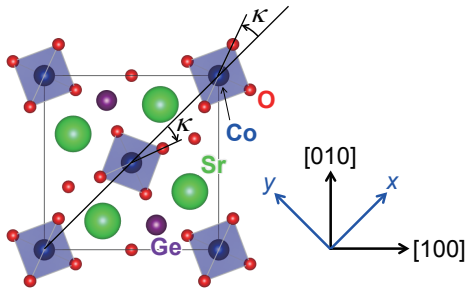


FIG. 1. (a) The schematic crystal structure of SCGO projected onto the  $ab$ -plane.

\* akaki@ahmf.sci.osaka-u.ac.jp

nance (ESR) technique supported by theoretical calculations, we show that, due to its isotropic nature, Sr<sub>2</sub>CoGe<sub>2</sub>O<sub>7</sub> (SCGO) exhibits a purely quadrupolar two-magnon mode in high magnetic fields. Measuring in different geometries for both Faraday and Voigt configurations, we find that this magnetically inactive excitation can only be excited by specific components of the oscillating electromagnetic field, in full agreement with the predictions of the relativistic metal-ligand hybridization.

## II. MAGNETOELECTRIC COUPLING AND THE HAMILTONIAN IN ÅKERMANITES

### A. Magnetolectric coupling

In åkermanites the spin vector chirality  $\hat{\mathbf{S}}_i \times \hat{\mathbf{S}}_j$  vanishes and the exchange interaction is uniform for each bond disabling the spin current or exchange striction as the origin of spin induced polarization. Instead, spin-dependent metal-ligand hybridization has been put forward as the source of finite polarization, induced by on-site second order spin-terms, in contrast to the aforementioned concepts which involve two neighboring spins.

The absence of the inversion on the magnetic ion site allows for the following general form for the  $\alpha = x, y, z$  components of the electric polarization at site  $\mathbf{r}$ ,

$$P_{\mathbf{r}}^{\alpha} = \sum_{\beta, \gamma \in x, y, z} c_{\beta\gamma}^{\alpha} \hat{S}_{\mathbf{r}}^{\beta} \hat{S}_{\mathbf{r}}^{\gamma}, \quad (1)$$

where the  $\hat{S}_{\mathbf{r}}^{\beta}$  and  $\hat{S}_{\mathbf{r}}^{\gamma}$  are the spin components at the same site  $\mathbf{r}$ , and  $c_{\beta\gamma}^{\alpha} = c_{\gamma\beta}^{\alpha}$  with  $\sum_{\beta} c_{\beta\beta}^{\alpha} = 0$  is a traceless  $3 \times 3 \times 3$  tensor symmetric in the lower two indices, effectively coupling the polarization to a time reversal invariant spin-quadrupole operators. The symmetry properties of the crystal reflected by the local environment of the magnetic ions determine the explicit form of tensor  $c_{\beta\gamma}^{\alpha}$  resulting in the following spin-induced polarization characteristic for the åkermanite family [11, 17, 18]:

$$\begin{pmatrix} P_j^x \\ P_j^y \end{pmatrix} \propto \begin{pmatrix} -\cos 2\kappa & -(-1)^j \sin 2\kappa \\ -(-1)^j \sin 2\kappa & \cos 2\kappa \end{pmatrix} \cdot \begin{pmatrix} \hat{Q}_j^{2xx} \\ \hat{Q}_j^{2yz} \end{pmatrix}, \quad (2a)$$

transforming as a two-dimensional irreducible representation of the point group, and

$$P_j^z \propto -\cos 2\kappa \hat{Q}_j^{x^2-y^2} - (-1)^j \sin 2\kappa \hat{Q}_j^{2xy}, \quad (2b)$$

a one-dimensional irreducible representation. The  $(-1)^j$  accounts for the alternation of the angle  $\kappa \approx \pm 20.5^\circ$  on the two sublattices and  $\kappa$  measures the rotation of the oxygen tetrahedra around the cobalt ions with respect to the [110] direction, as indicated in Fig. 1. The  $\hat{Q}$  operators represent a symmetric combination of the spin operators

$$\hat{Q}_j^{2\alpha\beta} = \hat{S}_j^{\alpha} \hat{S}_j^{\beta} + \hat{S}_j^{\beta} \hat{S}_j^{\alpha} \quad (3)$$

and

$$\hat{Q}_j^{x^2-y^2} = (\hat{S}_j^x)^2 - (\hat{S}_j^y)^2. \quad (4)$$

They are spin-quadrupole operators, satisfying the

$$\sum_{\mu=x, y, z} \left[ \left[ \hat{Q}_j^{2\alpha\beta}, \hat{S}_j^{\mu} \right], \hat{S}_j^{\mu} \right] = k(k+1) \hat{Q}_j^{2\alpha\beta} \quad (5)$$

property of a rank- $k$  tensor operator with  $k = 2$ . Note that the spin quadrupole operators in Eq. (2) may excite bimagnons (which are denoted by  $\mathbf{Q}$  further on) – this is in contrast with the spin-current mechanism, where the magnetoelectric coupling involves a bilinear, but spin-dipole operator only (a tensor operator with  $k = 1$ ). This expression is also obtained from the metal-ligand hybridization mechanism [9] as

$$\mathbf{P}_j \propto \sum_{i=1}^4 \mathbf{e}_{i,j} \left[ 3(\mathbf{e}_{i,j} \cdot \hat{\mathbf{S}}_j)^2 - \hat{\mathbf{S}}_j^2 \right], \quad (6)$$

where the sum is over the four oxygens surrounding the Co magnetic ion at site  $j$  and  $\mathbf{e}_{i,j}$  denotes the unit vector pointing from the Co ion to the  $i$ -th O ion. The  $\mathbf{P}_j$  as defined above is a traceless operator in the spin Hilbert space.

### B. Model Hamiltonian

As indicated by magnetic studies [19] and neutron dispersion measurements [18, 20], the cobalt planes are only weakly coupled in åkermanites. We consider the following 2D spin Hamiltonian as a minimal microscopic model for SCGO,

$$\begin{aligned} \mathcal{H} = & J \sum_{(i,j)} \left( \hat{S}_i^x \hat{S}_j^x + \hat{S}_i^y \hat{S}_j^y \right) + J_z \sum_{(i,j)} \hat{S}_i^z \hat{S}_j^z \\ & + J_{pz} \sum_{\langle i,j \rangle} P_i^z P_j^z + \Lambda \sum_i (\hat{S}_i^z)^2 \\ & - \mu_B \sum_i [g_{ab}(H_x \hat{S}_i^x + H_y \hat{S}_i^y) + g_c H_z \hat{S}_i^z], \quad (7) \end{aligned}$$

where  $J$  and  $J_z$  are the anisotropic exchange constants between the nearest neighbor spins,  $\Lambda > 0$  is the single ion anisotropy, and  $J_{pz}$  is the antiferroelectric coupling. We neglect the Dzyaloshinskii-Moriya interactions and off diagonal components of the  $g$ -tensor, which are rather small even in more anisotropic åkermanites, and show that both static and dynamical properties can be reproduced for isotropic exchange interaction  $J = J_z$  and with small single-ion anisotropy  $\Lambda \sim J$ .

Without the  $J_{pz}$  term the Hamiltonian represents an easy plane antiferromagnet with a Goldstone mode ( $\Delta_1 = 0$ ). A finite  $J_{pz}$  was introduced for Ba<sub>2</sub>CoGe<sub>2</sub>O<sub>7</sub> to explain the vanishing of electric polarization in zero field [17] and the absence of Goldstone modes in the neutron scattering study [18]. At zero magnetic field, the

electric polarization is also zero in SCGO (Fig. 2(b)), hence the ground state must be an antiferroelectric state, selecting [100] as the magnetic easy axis within the easy plane.

### III. SAMPLE CHARACTERIZATION, EXPERIMENTAL DETAILS

We grew single crystalline samples of SCGO using the floating zone method. Room temperature X-ray diffraction measurements confirmed the tetragonal  $P4_2m$  structure with no impurity phases. All the samples used for the experiments were cut along the crystallographic principal axes to make samples with plate-like shapes after checking by the X-ray back-reflection Laue technique.

The magnetization was measured in static magnetic fields of up to 7 T using a commercial SQUID magnetometer and by the induction method, using a coaxial pick-up coil, in pulsed fields of up to 55 T, with a pulse duration of 7 millisecond.

The electric polarization induced by magnetic fields was obtained by integrating the polarization current as a function of time. Since in  $\text{\AA}$ kermanite materials electric polarization emerges even without applying poling electric fields, which is a unique feature of their multiferroicity [8, 11–13], we measured the polarization current without poling electric fields.

Low-field ESR spectra up to 14 T at 1.5 – 1.6 K and for frequencies below 500 GHz were taken using a home-made transmission ESR cryostat in a superconducting magnet.

High-field ESR measurements at 1.4 K in pulsed magnetic fields of up to 55 T were conducted by utilizing a far-infrared laser and Gunn oscillators (75, 90, 95, 110, and 130 GHz) coupled with a frequency doubler to generate sub-millimeter and millimeter waves. We used an InSb bolometer as a detector. All the experiments were carried out using unpolarized light. Figure. 3 shows the schematic experimental setup of the ESR spectrometer in pulsed magnetic fields.

### IV. STATIC PROPERTIES AND MAGNETIC ANISOTROPY

In order to obtain information about the magnetic anisotropies, we measured the magnetization and the induced electric polarization as function of external magnetic field. The results of our measurements, taken at 1.4 K, well below the Néel temperature of 6.5 K [19], are displayed in Fig. 2.

#### A. Magnetization

The magnetization in the cobalt plane, (001), rises almost linearly with magnetic field, reaching saturation at

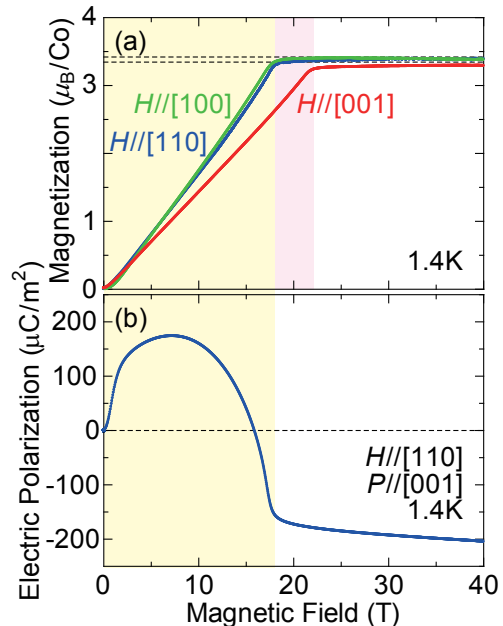


FIG. 2. (a) Magnetic field dependence of magnetization in SCGO at 1.4 K. Dashed lines indicate the saturation magnetization values using  $g_{ab} = 2.28$  and  $g_c = 2.23$ , obtained from the ESR measurements [see Eqs.(25c) and (25a)], for the in-plane and out-of-plane components, respectively. (b) Magnetic field dependence of the out-of-plane component of induced electric polarization ( $P_c$ ) at 1.4 K in the case of  $\mathbf{H}||[110]$ . Above saturation, the polarization and magnetization become flat. Yellow and pink shaded areas mark the phases below saturation for in-plane and out-of-plane magnetic fields, respectively.

3.42  $\mu_B/\text{Co}$  just above 18 T. Along the perpendicular [001] direction, the corresponding values are 3.3  $\mu_B/\text{Co}$  and 21.6 T, providing  $g_{ab} \approx 2.3$  and  $g_c \approx 2.2$  (we will get a more precise values from fitting the ESR spectra in Sec. V C). The magnetization curves are nearly isotropic, and the difference in the saturation fields is mainly explained by the  $g$ -tensor anisotropy. In other  $\text{\AA}$ kermanite compounds, like  $\text{Sr}_2\text{CoSi}_2\text{O}_7$  [8] and  $\text{Ba}_2\text{CoGe}_2\text{O}_7$  [21], the slope of in-plane magnetization is almost twice the slope of the magnetization measured perpendicular to the cobalt plane. This large difference signals the presence of large easy-plane anisotropy. Here, the discrepancy between the slopes of in-plane and out-of-plane magnetization is small, and can be accounted for by a smaller  $g$ -tensor anisotropy and a smaller easy-plane anisotropy.

To quantify how different the magnetic anisotropies are in SCGO compared to the sister materials, let us take a look at the saturation fields. As shown in the Appendix A 3 and A 4, the saturation fields from a mean field approach can be expressed as  $\mu_B g_{ab} H_{xy}^{\text{sat}} = 12J$  and  $\mu_B g_z H_z^{\text{sat}} = 6J + 6J_z + 2\Lambda$  for the in-plane and out-of-plane magnetic field directions. We can easily utilize this discrepancy in the saturation fields to get an estimate for

the easy-plane and exchange anisotropies:

$$6(J_z - J) + 2\Lambda = \mu_B g_c H_z^{\text{sat}} - \mu_B g_{ab} H_{xy}^{\text{sat}}. \quad (8)$$

Assuming (which will be justified in our fitting of the ESR data) a negligibly small exchange anisotropy, we get  $\Lambda \approx 2.2$  K for SCGO, while for  $\text{Ba}_2\text{CoGe}_2\text{O}_7$  for example, the difference in saturation fields in the easy plane, (001), and hard axis direction, [001], is about 20 T, resulting in an order of magnitude larger anisotropy of 13 K [22].

The ratio  $\Lambda/J$  is closely related to the spin length (more precisely, the size of the ordered moment in the mean field approximation), larger anisotropy results in greater spin reduction:

$$\langle S \rangle = \frac{3}{2} \left[ 1 - \left( \frac{\Lambda}{12J} \right)^2 \right] \quad (9)$$

In SCGO  $\Lambda/J$  is an order of magnitude smaller than in the other  $\ddot{\text{a}}$ kermanites [15, 22], leaving the spins nearly in a pure 3/2 state and keeping the dipole and quadrupole characters of the excited modes well separated here.

The magnetization shown here is the measured one, the van-Vleck term is not subtracted. The magnetization above the saturation field is very flat, the van-Vleck paramagnetic susceptibility is vanishingly small. This is in accord with the small anisotropies, as the level splitting of  $t_2$  orbital is small and the  $\text{CoO}_4$  tetrahedra are weakly distorted [23].

## B. Electric polarization

The behavior of electric polarization as a function of magnetic field is nearly the same as in other  $\ddot{\text{a}}$ kermanites [8, 11]. However, subtle deviations provide additional proof of a smaller easy-plane anisotropy. When the field is applied in the  $ab$  cobalt plane, the polarization has only out-of-plane component, *i.e.* only  $P^z$  is finite. Such measurement is shown in Fig. 2(b) as a function of magnetic field. The inflection point of the polarization curve at 18 T signals the transition to the saturated phase. Before reaching the transition point the spins are turning within the cobalt-plane towards the field direction, in this case towards [110]. Due to the easy plane anisotropy, they are not fully grown 3/2 spins, but somewhat shorter, see Eq. (9). As they turn towards the field, the polarization changes, reaching its extrema when the spins are parallel to one of the tetrahedron edges. Note that if the tetrahedra were not rotated, *i.e.* if  $\kappa$  were zero, the polarization would have its extrema when the spins are aligned with [110] and  $[\bar{1}10]$ . At the transition field, the spins do not rotate any further, but the magnetic field, now strong enough to compete with the anisotropy, stretches them to asymptotically reach their maximal 3/2 value. This behavior can be nicely seen in magnetization measurements in the other members of the  $\ddot{\text{a}}$ kermanite family, as the magnetization after saturation

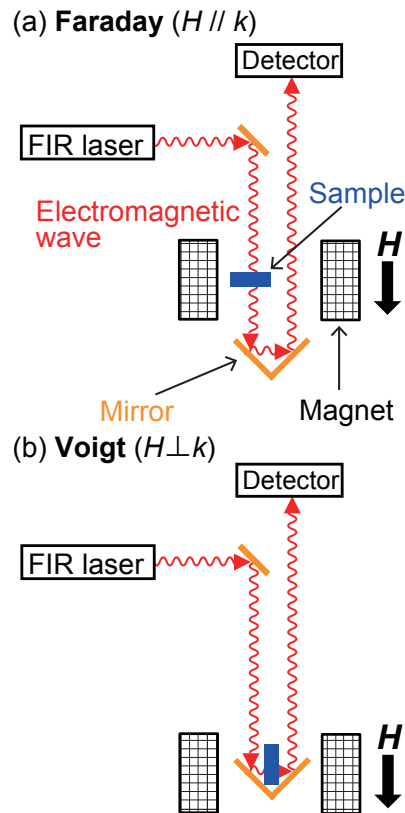


FIG. 3. Schematic experimental setup for the high-field ESR measurements, with different light configurations.

is not a completely field independent constant, but further increases towards the full saturation value [8, 21]. This is also apparent in the polarization curve which decreases slowly after the transition instead of becoming flat [8]. More prominent changes of these observables after the saturation indicate that the spins are further away from being fully grown, and consequently that the material has larger single-ion anisotropy. In the case of SCGO, this decay in  $P^z$  and climb in the magnetization is significantly smaller than those in  $\text{Sr}_2\text{CoSi}_2\text{O}_7$  and  $\text{Ba}_2\text{CoGe}_2\text{O}_7$ , further evidencing a smaller anisotropy.

To conclude on the experimental observations of the static properties, SCGO has, similarly to its sister compounds, easy-plane single ion anisotropy, supporting a planar antiferromagnetic configuration of cobalt spins in agreement with neutron powder diffraction measurements [19]. However, both magnetization and polarization data indicate that the anisotropy is about an order of magnitude smaller than those in the previously studied compounds, and the spin lengths in the ground state are much closer to the isotropic 3/2 value.

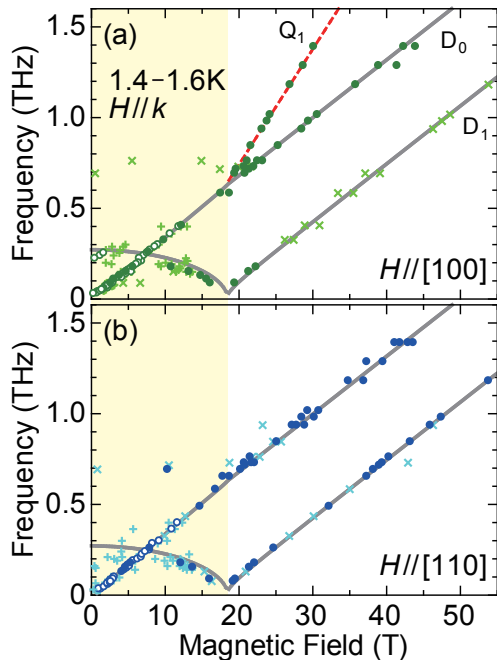


FIG. 4. Frequency-field diagrams of the ESR resonance fields of  $\text{Sr}_2\text{CoGe}_2\text{O}_7$  for magnetic fields parallel to the (a) [100] and (b) [110] directions. Open circles (plus) are strong (weak) resonance signals obtained from the measurements in static fields at 1.6 K, while solid circles (cross) show strong (weak) resonance signals in pulsed fields at 1.4 K. The solid lines represent the resonance modes from the multiboson spin-wave theory, using the following set of parameters:  $g_c = 2.23$ ,  $g_{ab} = 2.28$ ,  $J = 49.1$  GHz,  $J_z = 45.0$  GHz, and  $\Lambda = 49.7$  GHz. The red dashed line in (a) indicates a resonance mode with a slope twice larger than the others, corresponding to a two-magnon excitation. Yellow shaded area marks the phase below saturation for in-plane magnetic fields.

## V. DYNAMIC PROPERTIES STUDIED BY ELECTRON SPIN RESONANCE

We continue our study with the dynamical properties. The ESR measurements have been performed for two configurations. In the Faraday configuration, the exciting electromagnetic wave propagates with wave vector  $\mathbf{k}$  in the direction of the external magnetic field ( $\mathbf{H} \parallel \mathbf{k}$ ), consequently in this configuration we can observe excitations driven by the components of electromagnetic field which are perpendicular to the external magnetic field. In the Voigt configuration, the electromagnetic wave propagates in a perpendicular direction with respect to the external magnetic field ( $\mathbf{H} \perp \mathbf{k}$ ), and the excitation spectrum contains electric and magnetic transitions both parallel and perpendicular to the applied field. Therefore, above the saturation, when the spins are aligned with the field, the Faraday configuration displays transitions driven by electric and magnetic components perpendicular to the spins, while the spectrum in the Voigt configuration contains both parallel and perpendicular components with

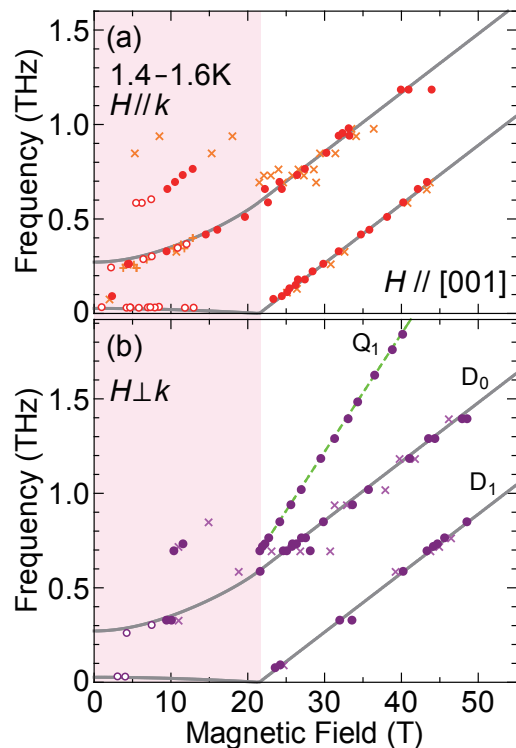


FIG. 5. Frequency-field diagrams of the ESR resonance fields of  $\text{Sr}_2\text{CoGe}_2\text{O}_7$  for magnetic fields parallel to the [001] directions in the (a) Faraday and (b) Voigt configuration, showing the two-magnon absorptions (green squares). Open circles (plus) are strong (weak) resonance signals obtained from the measurements in static fields at 1.6 K, while solid circles (cross) show strong (weak) resonance signals in pulsed fields at 1.4 K. The solid lines represent the resonance modes calculated by the multiboson spin-wave theory with the same set of parameters as in Fig. 4. The shaded area in red is the magnetic field range below the saturation field.

respect to the spin orientation. In both configurations we measure the ESR spectra for external magnetic fields parallel to [100], [110] and [001] crystallographic directions, having in total six different geometries. Measurements in different setups allow for the experimental verification of selection rules and identification of the observed excitations.

### A. Frequency-magnetic field plots of the resonance fields

Figures 4 and 5(a) shows the frequency-magnetic field plots of ESR resonance fields at 1.4 – 1.6 K in the Faraday configuration ( $\mathbf{H} \parallel \mathbf{k}$ ). At zero-field, three energy gaps are clearly identified:  $\Delta_1 \approx 27$  GHz,  $\Delta_2 \approx 220$  GHz, and  $\Delta_3 \approx 700$  GHz. The gaps close to  $\Delta_2$  and  $\Delta_3$  were also reported in THz spectroscopy measurements of  $\text{Ba}_2\text{CoGe}_2\text{O}_7$  [14, 22], corresponding to transversal and longitudinal spin excitations, respectively. We can trace the origin of  $\Delta_2$  to the interplay of exchange interaction

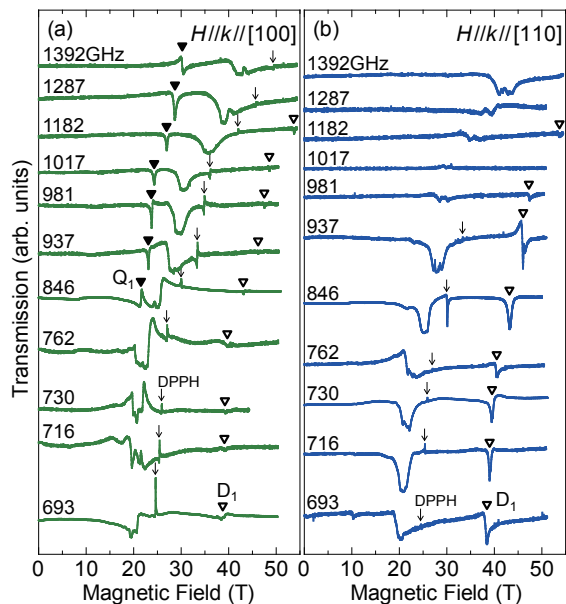


FIG. 6. Frequency dependent ESR absorption spectra of SCGO in Faraday configuration at 1.4 K for (a)  $H||[100]$  and (b)  $H||[110]$ . Arrows mark the resonance fields of DPPH (2,2-diphenyl-1-picrylhydrazyl, ESR marker with  $g = 2.0036$ ). Open and solid triangles mark the resonance fields of one-magnon ( $D_1$ ) and two-magnon ( $Q_1$ ) resonance modes, respectively. For Faraday configuration and the two in-plane static field direction, the  $D_1$  dipolar and  $Q_1$  quadrupolar transitions appear to be mutually exclusive.

and single-ion easy-plane anisotropy and  $\Delta_3$  to the exchange interaction [15, 22, 24].

The magnetic field dependence of the excitations below 500 GHz clearly resembles the usual ESR spectra for the easy-plane antiferromagnets [25]. The only difference is the emergence of the smallest gap,  $\Delta_1$ . This additional gap  $\Delta_1$  is the result of a small anisotropy that fully breaks the spin rotational symmetry — also breaking the remaining  $O(2)$  symmetry within the easy plane — and can be explained by introducing polarization-polarization interaction which is also responsible for the vanishing of induced  $P^z$  as the magnetic field approaches zero [17]. Similar energy gap has been observed in inelastic neutron diffraction measurements of  $\text{Ba}_2\text{CoGe}_2\text{O}_7$  [18].

Above the saturation, the modes are linearly increasing with the magnetic field, providing further evidence for a smaller anisotropy. We can identify the conventional magnon modes,  $D_0$  and  $D_1$  with the slopes corresponding to the  $g$  factors we obtained from the magnetization measurements discussed in Sec. IV A. In the case of  $H||[100]$ , however, an additional mode,  $Q_1$ , emerges at higher frequencies, its frequency increasing twice as fast with magnetic field as for the dipolar transitions,  $D_0$  and  $D_1$ . This rapidly increasing mode corresponds to the absorption of two magnons.

Such two-magnon excitation can be considered as a quadrupolar fluctuation. The quadrupole operators

are second order in spin operators, allowing for on-site  $\Delta S^z = 2$  bimagnon creation and the necessary preservation of time reversal invariance. As a consequence, quadrupole operators transforming the same way as the components of the polarization vector for a given symmetry group can couple to the corresponding electric field components. Here and in the next section we will argue that this is what happens in our measurement. The  $Q_1$  bimagnon mode becomes visible in the spectrum due to the quadrupole transitions driven by the oscillating electric field of the light, even when  $Q_1$  does not have dipole component but is purely quadrupolar.

Figure 6 displays the ESR absorption spectra of SCGO at 1.4 K in Faraday configuration. The  $Q_1$  bimagnon mode is visible for  $H||[100]$  only, as observed when comparing Fig. 4 (a) and (b). The signal intensities of the  $D_1$  mode show a negligible absorption for  $H||[100]$  and a strong absorption for  $H||[110]$ . It appears that the absorptions by the  $D_1$  and  $Q_1$  modes are mutually exclusive for these setups.

## B. Calculation of the one- and two-magnon spectra in high magnetic fields

Here we present our analytical results for the excitation energies in high magnetic fields above the saturation. For simplicity we neglect the  $J_{pz}$  term in the Hamiltonian (7), since we expect it to be very small. We note that Appendix A contains analytical solutions of a variational approach and multiboson spin-wave theory for the entire spectra, including the low field regime as well.

### 1. Excitations for the magnetic field $||[001]$

When the external magnetic field is parallel to the  $[001]$  direction (*i.e.* perpendicular to the  $(001)$  easy plane), the Hamiltonian shown in Eq. (7) conserves the number of magnons. The ground state above the saturation is the trivial product of the  $|S^z = 3/2\rangle$  states over all the sites. We need to invest  $g_c\mu_B H_z - 2\Lambda - 6J_z$  diagonal energy to

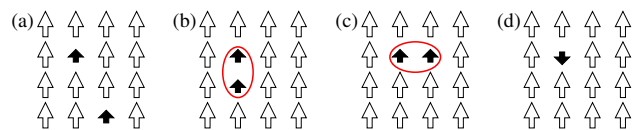


FIG. 7. (a) A typical two-magnon configuration, short black arrows show the  $S^z = 1/2$  spins moving on the  $S^z = 3/2$  spin background (empty arrows). The  $\mathbf{q} = (\pi, \pi)$  linear combinations of the neighboring  $S^z = 1/2$  spin states shown in (b) and (c) are exact eigenstates, and they make the twofold degenerate  $\mathbf{B}_1$  bound state. (d) The down-pointing short arrow represents a  $S^z = -1/2$  state; the  $\mathbf{q} = (\pi, \pi)$  linear combination of such states is the  $Q_1$  mode (see Eq. (15)), which is also an eigenstate for the model with nearest neighbor exchanges only.

create a single magnon, the  $|S^z = 1/2\rangle$  spin state on a site  $j$  with the  $\hat{S}_j^-$  operator. This spin state can then hop with amplitude  $3J/2$  to neighboring sites. The resulting state is described by the

$$|D(\mathbf{q})\rangle = \sum_j e^{i\mathbf{q}\cdot\mathbf{r}_j} \hat{S}_j^- |\text{GS}\rangle \quad (10)$$

wave function, with energy

$$\omega_1(\mathbf{q}) = \mu_B g_c H_z - 2\Lambda - 6J_z + 6J\gamma_{\mathbf{q}}, \quad (11)$$

where  $\gamma_{\mathbf{q}}$  is the geometrical factor  $\frac{1}{2}(\cos q_x + \cos q_y)$ . We plot the dispersion above in Fig. 8(a) for a realistic ratio of parameters  $J = J_z = \Lambda$ , which is very close to the one we will get for SCGO below, in Sec. V C.

Due to the alternation of the tetrahedra, the unit cell is doubled, so magnons at both  $\mathbf{q} = (0, 0)$  and  $\mathbf{q} = (\pi, \pi)$  wave vectors are excited in the ESR spectrum (note that the unit cell of the Hamiltonian contains only one spin), with energy

$$\omega_{D_0} \equiv \omega_1(0, 0) = \mu_B g_c H_z - 2\Lambda - 6J_z + 6J, \quad (12)$$

$$\omega_{D_1} \equiv \omega_1(\pi, \pi) = \mu_B g_c H_z - 2\Lambda - 6J_z - 6J. \quad (13)$$

The energy difference between these two modes is simply the bandwidth of the magnons, equal to  $12J$ .

Two magnons can propagate freely with the dispersion given above, except when they meet at neighboring sites (Fig. 7(b) and (c)). Furthermore, the two magnons can hop onto each other, creating an  $|S^z = -1/2\rangle$  spin state on a single site (Fig. 7(d)). This leads to an interaction between the magnons, and we need to solve the corresponding two-body problem. While this can be done analytically [26–30], here we resort to exact diagonalization in the two-magnon Hilbert space, and plot the spectrum for finite clusters. In Fig. 8(b), we show the result compiled from different size clusters (up to 3200 sites), which respect the full  $D_4$  symmetry of the square lattice. The propagating magnons form a two magnon continuum. The continuum is the broadest at the center of the Brillouin zone, where its width of  $24J$  is twice the bandwidth of the magnons, and shrinks to a single, highly degenerate point at the  $\mathbf{q} = (\pi, \pi)$  corner of the Brillouin zone, with energy

$$\omega_2^{\text{cont.}}(\pi, \pi) = 2\mu_B g_c H_z - 4\Lambda - 12J_z. \quad (14)$$

We observe that close to  $\mathbf{q} = (\pi, \pi)$ , three distinct state split off from the two-magnon continuum due to the interaction. In fact, at  $\mathbf{q} = (\pi, \pi)$  the

$$|Q_1\rangle = \sum_j (-1)^j \hat{S}_j^- \hat{S}_j^- |\text{GS}\rangle \quad (15)$$

state (shown in Fig. 7(d)), with energy

$$\omega_{Q_1} = 2\mu_B g_c H_z - 2\Lambda - 12J_z, \quad (16)$$

is decoupled from the other states [29]. So are the configurations having two neighboring  $|+1/2\rangle$  states in either of the directions [Fig. 7(b) and (c)], with energy

$$\omega_{B_1} = 2\mu_B g_c H_z - 4\Lambda - 11J_z. \quad (17)$$

The twofold degeneracy of this state is lifted as we go away from the  $\mathbf{q} = (\pi, \pi)$  point [26, 27], as shown in Fig. 8(c).

## 2. Excitations for the external magnetic field in the (001) easy plane

When the field is along the [100] or [110] direction, the Zeeman term and the exchange term in Hamiltonian (7) do not commute any more. Instead, we can resort to perturbation expansion. We assume a large

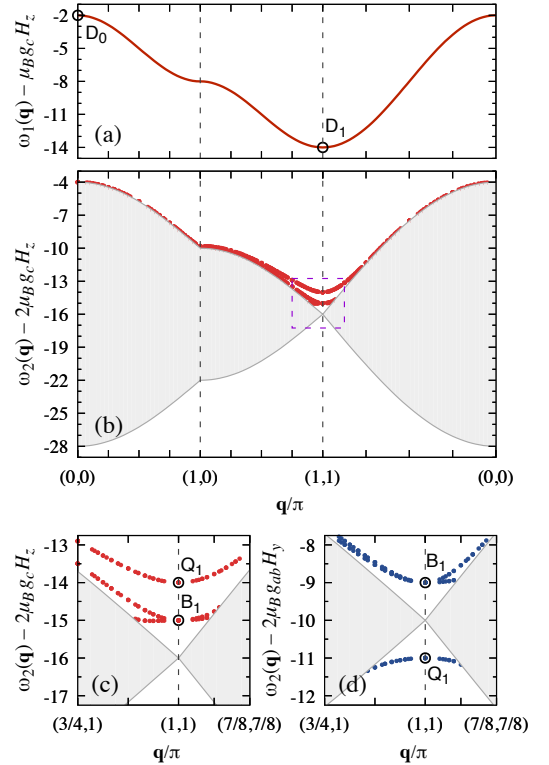


FIG. 8. One- and two-magnon spectra in magnetic field above the saturation for  $\Lambda = 1$  and  $J = J_z = 1$ . (a) The dispersion of a single magnon along a path in the 2-dimensional Brillouin zone, following Eq. (11). (b) In the two-magnon spectrum, the gray shaded area is the two-magnon continuum, the red points outside the continuum are the antibound states obtained from diagonalizing the two-magnon problem on different size clusters. (c) and (d) shows the magnified part of the two magnon spectrum close to  $\mathbf{q} = (\pi, \pi)$ . The field is along the [001] direction in the (a),(b), and (c), while it lies within the easy (001) plane in (d). The circles show the energy of the  $D_0$  and  $D_1$  mode in (a) and the energy of the  $B_1$  and  $Q_1$  mode in (c) and (d).

magnetic field in the  $y$  direction below and we rewrite the Hamiltonian  $\mathcal{H}$  using a new basis for the spin operators:  $(\hat{S}^x, \hat{S}^y, \hat{S}^z) \rightarrow (\tilde{S}^y, \tilde{S}^z, \tilde{S}^x)$ , so that the quantization axis is along the magnetic field (the spectra do not depend on the actual direction of the field in the  $xy$  plane, as the anisotropy has an  $O(2)$  symmetry about the  $z$  axis when  $J_{pz} = 0$ ). We can write the Hamiltonian as  $\mathcal{H} = \mathcal{H}_0 + \mathcal{H}_1$ , where  $\mathcal{H}_0$  is diagonal in the new basis,

$$\mathcal{H}_0 = \frac{\Lambda}{2} \sum_i \left( \frac{15}{4} - \tilde{S}_i^z \tilde{S}_i^z \right) + J \sum_{(i,j)} \tilde{S}_i^z \tilde{S}_j^z - \mu_B H_y g_{ab} \sum_i \tilde{S}_i^z, \quad (18)$$

and  $\mathcal{H}_1$  contains the off-diagonal matrix elements,

$$\begin{aligned} \mathcal{H}_1 &= \frac{J_z + J}{4} \sum_{(i,j)} \left( \tilde{S}_i^- \tilde{S}_j^+ + \tilde{S}_i^+ \tilde{S}_j^- \right) \\ &+ \frac{\Lambda}{4} \sum_i \left( \tilde{S}_i^- \tilde{S}_i^- + \tilde{S}_i^+ \tilde{S}_i^+ \right) \\ &+ \frac{J_z - J}{4} \sum_{(i,j)} \left( \tilde{S}_i^- \tilde{S}_j^- + \tilde{S}_i^+ \tilde{S}_j^+ \right). \end{aligned} \quad (19)$$

Below we perform a first order degenerate perturbation expansion using the  $\mathcal{H}_1$  as a perturbation operator. The ground state of the  $\mathcal{H}_0$  operator is a ferromagnetic state with all the spins pointing along the field. The  $\tilde{S}_i^- \tilde{S}_i^-$  and  $\tilde{S}_i^+ \tilde{S}_j^+$  processes, which change the number of magnons, first appear in the second order of perturbation expansion, and we neglect them in the following, assuming a small single-ion anisotropy and nearly isotropic exchange. Within this approximation, the problem is equivalent with the one we discussed in the previous subsection for  $\mathbf{H} \parallel [001]$ , but we need to replace  $J$  by  $(J + J_z)/2$ ,  $J_z$  by  $J$ , and the on site anisotropy  $\Lambda$  by  $-\Lambda/2$  in all of Eqs. (11)-(17). Most notably, the sign of the effective anisotropy changes. The dispersion of single magnon then becomes

$$\omega_1(\mathbf{q}) = \mu_B g_{ab} H_y + \Lambda - 6J + (3J + 3J_z) \gamma_{\mathbf{q}} + \dots, \quad (20)$$

where the dots denote neglected higher order terms. Continuing the replacements, we get

$$\omega_{D_0} = \mu_B g_{ab} H_y + \Lambda - 3J + 3J_z + \dots, \quad (21a)$$

$$\omega_{D_1} = \mu_B g_{ab} H_y + \Lambda - 9J - 3J_z + \dots, \quad (21b)$$

$$\omega_2^{\text{cont.}}(\pi, \pi) = 2\mu_B g_{ab} H_y + 2\Lambda - 12J + \dots, \quad (21c)$$

$$\omega_{Q_1} = 2\mu_B g_{ab} H_y + \Lambda - 12J + \dots, \quad (21d)$$

$$\omega_{B_1} = 2\mu_B g_{ab} H_y + 2\Lambda - 11J + \dots. \quad (21e)$$

The  $Q_1$  is now below the continuum (for  $\Lambda > 0$ ), as shown in Fig. 8(d), forming a bound state.

The difference between the dipolar and quadrupolar modes is illustrated schematically in Fig. 9. Denoting by  $S^{\parallel}$  the spin component parallel to the external field

and by  $S^{\perp 1}$  and  $S^{\perp 2}$  the two orthogonal components, the expectation value of the spin operators are

$$\begin{aligned} \langle \hat{S}^{\perp 1} \rangle &\propto (-1)^j \sin(\omega_{D_1} t), \\ \langle \hat{S}_j^{\perp 2} \rangle &\propto (-1)^j \cos(\omega_{D_1} t), \\ \langle \hat{S}_j^{\parallel} \rangle &\approx \frac{3}{2} \end{aligned} \quad (22)$$

in the  $D_1$  dipolar mode. They describe the usual precession of dipolar components of the spin [green arrows in Fig. 9(a) and (c)] around the magnetization axes. In the  $Q_1$  quadrupolar mode, the  $\langle S^{\perp 1} \rangle = \langle S^{\perp 2} \rangle = 0$ , instead the

$$\begin{aligned} \langle \hat{Q}_j^{2\perp 1\perp 2} \rangle &\propto (-1)^j \sin(\omega_{Q_1} t), \\ \langle \hat{Q}_j^{\perp 1\perp 1\perp 2} \rangle &\propto (-1)^j \cos(\omega_{Q_1} t) \end{aligned} \quad (23)$$

$$\begin{aligned} \langle \hat{Q}_j^{2\perp 1\perp 1'} \rangle &\propto (-1)^j \sin(\omega_{Q_1} t), \\ \langle \hat{Q}_j^{\perp 1\perp 1'\perp 2} \rangle &\propto (-1)^j \cos(\omega_{Q_1} t) \end{aligned} \quad (24)$$

components of the quadrupolar moment [shown as a green ellipse in Fig. 9(b) and (d)] rotate around the static dipolar moment aligned with the external magnetic field.

### C. Fitting the parameters

We will use the modes linear in magnetic field above saturation in Figs. 4 and 5 to extract parameters of the Hamiltonian. The  $\omega_{D_1}$  and  $\omega_{Q_1}$  modes show a narrow absorptions in Figs. 6 and 10, while the  $\omega_{D_0}$  resonance mode is broad, giving us a natural choice of selecting the narrow  $\omega_{D_1}$  (solid circles in Fig. 4(b) for  $\mathbf{H} \parallel [110]$  and 5(a) for  $\mathbf{H} \parallel [001]$ ) and  $\omega_{Q_1}$  modes (solid circles in Fig. 4(a) for  $\mathbf{H} \parallel [100]$  and 5(b) for  $\mathbf{H} \parallel [001]$ ) to determine the precise values of the  $\Lambda$ ,  $J$ ,  $J_z$ , and the  $g$  values.

Performing a standard multiple linear regression fit using Eqs. (13), (16), (21b), and (21d) as a model, we get the following parameters for the  $g$  values,

$$g_{D_1}^{[001]} = 2.23 \pm 0.02, \quad (25a)$$

$$g_{Q_1}^{[001]} = 4.42 \pm 0.02, \quad (25b)$$

$$g_{D_1}^{[110]} = 2.28 \pm 0.01, \quad (25c)$$

$$g_{Q_1}^{[100]} = 4.57 \pm 0.02, \quad (25d)$$

where, instead of  $g_{ab}$  and  $g_c$ , we left the  $g$ -values of the corresponding modes as free parameters which measure the slope. The values of the exchange couplings and on-site anisotropy are

$$J = 49.1 \pm 0.8 \text{ GHz} = 2.36 \pm 0.04 \text{ K}, \quad (26a)$$

$$J_z = 45.0 \pm 1.1 \text{ GHz} = 2.16 \pm 0.05 \text{ K}, \quad (26b)$$

$$\Lambda = 49.7 \pm 4.2 \text{ GHz} = 2.39 \pm 0.20 \text{ K}. \quad (26c)$$

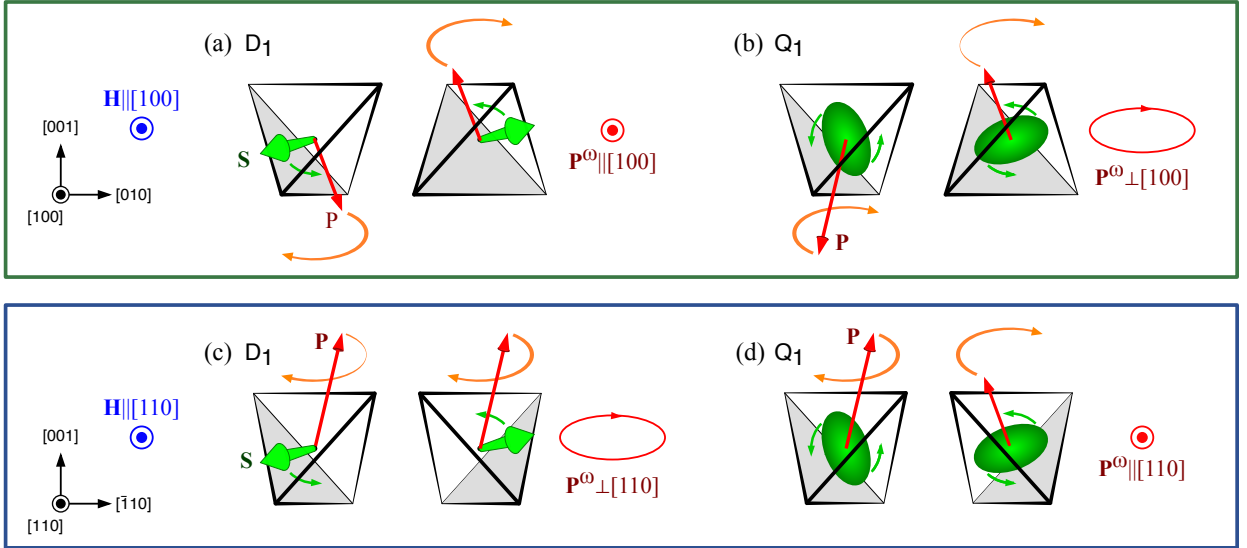


FIG. 9. Schematic plot of the dipolar [(a) and (c)] and quadrupolar [(b) and (d)] modes in different geometries, as seen from the direction of the magnetic field. In the dipolar wave  $D_1$  for  $\mathbf{H}||[110]$  (c) and the quadrupolar mode  $Q_1$  for  $\mathbf{H}||[100]$  (b) the oscillating component of the uniform electric polarization  $\mathbf{P}^\omega$  (shown by red ellipse) is perpendicular to the external magnetic field  $\mathbf{H}$ , therefore they are active in the Faraday configuration. In the  $D_1$  for  $\mathbf{H}||[100]$  (a) and  $Q_1$  for  $\mathbf{H}||[110]$  (d) the  $\mathbf{P}^\omega||\mathbf{H}$  (*i.e.* it oscillates in and out from the shown plane), so these modes are active in Voigt configuration only. The green ellipse represents the rotating quadrupolar moments, while the green arrows show the precessing dipolar spins on the two sublattices. The red arrows show the electric polarization vectors which are excited by the oscillating electric field. Animations of these modes are shown in Supplement [31]

The exchange parameter  $J$  is in perfect agreement with the measured shift between the two single-magnon modes,  $\omega_{D_0} - \omega_{D_1} = 12J \approx 600$  GHz in Fig. 5 [32]. The fit gives an  $\omega_{D_1} = 0$  intercept at  $16.6 \pm 0.1$  T, while for  $H||[001]$  the intercept  $21.5 \pm 0.3$  T coincides with the saturation field, 21.5 T (Figs. 2(a) and 5).

Along the  $[100]$  the signal of the  $D_1$  mode is quite weak, and the points are more scattered around the line. Consistently, the error of a linear fit is larger, we get  $g_{D_1}^{[100]} = 2.27 \pm 0.04$  for the slope and  $-524 \pm 23$  GHz for the zero field intercept. According to our theory, the dynamics of this weak mode is governed by Eq. (21b), like for the  $\omega_{D_1}^{[110]}$  mode. Replacing the fitted values given by Eqs. (26a)-(26c), for the intercept we get 527 GHz, which is well within the estimated error bars. Similarly, we can conclude, that  $g_{D_1}^{[110]} = g_{D_1}^{[001]}$  within error bars, *i.e.* the slope of the two modes is equal, and can be identified with the  $g_{ab}$ . We choose the more precise  $g_{ab} = g_{D_1}^{[110]} = 2.28 \pm 0.01$  value.

The fit supports the two-magnon origin of the  $Q_1$  excitations, as  $g_{Q_1}^{[001]} \approx 2g_{D_1}^{[001]}$ , so we can associate  $g_{D_1}^{[001]}$  with  $g_c$  and  $g_{Q_1}^{[001]}$  with  $2g_c$ . Furthermore the  $g_{Q_1}^{[100]}$  is twice the  $g_{D_1}^{[100]}$  within the error bars.

Finally, we calculated the the single-magnon modes  $D_0$  and  $D_1$  from the multiboson spin-wave theory [33] using the above set of parameters. Adding a small  $W_z^2 J_{pz}/k_B = 2.5 \times 10^{-5}$  K, the calculated and the mea-

sured modes show an excellent agreement, even in the low field regime, as shown in Figs. 4 and 5.

We determined the energies of the  $D_0$  and  $D_1$  modes explicitly in Eqs. A8 and A16 of the Appendix A. Inserting zero magnetic field, we obtain

$$\Delta_2 = (6J + \Lambda) \sqrt{2 \left( 1 + \frac{J_z}{J} - \frac{12J_z}{6J + \Lambda} \right)}, \quad (27)$$

Inserting the fitted parameter values of Eqs. (26) we get  $\Delta_2 = 287 \pm 15$  GHz. This is not too far away from the experimentally observed gap,  $\Delta_2 = 220$  GHz. The discrepancy can be due to the quantum fluctuations in the Néel state, which are neglected in the linear multiboson spin wave calculation.

Quite interestingly, the anisotropy gap from the multiboson spin-wave theory,  $\Delta_2 = \sqrt{24J\Lambda}$  in the leading order and assuming  $J = J_z$ , is different from the standard linear spin wave gap  $\Delta_2 = \sqrt{16J\Lambda S^2} = \sqrt{36J\Lambda}$ . In fact, going beyond the linear spin wave theory we start to see quantum correction, the anisotropy gap becomes  $\Delta_2 = \sqrt{16J\Lambda S(S-1/2)} = \sqrt{24J\Lambda}$  for  $S = 3/2$  [34], coinciding with the gap obtained from the multiboson spin-wave theory.

#### D. Comparison to $\text{Ba}_2\text{CoGe}_2\text{O}_7$

The  $\text{Ba}_2\text{CoGe}_2\text{O}_7$  is a member of the åkermanite family, where the on-site anisotropy is believed to be large,

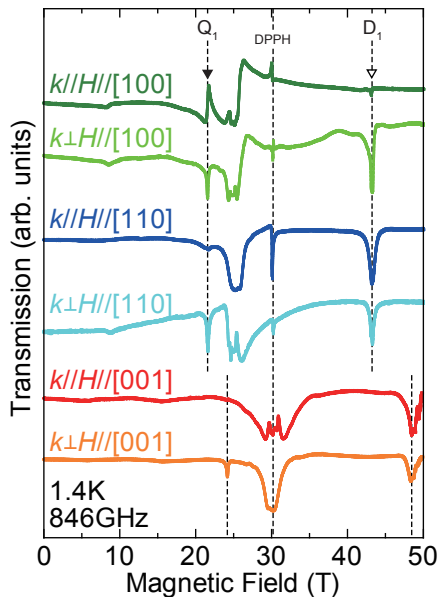


FIG. 10. ESR absorption spectra of  $\text{Sr}_2\text{CoGe}_2\text{O}_7$  at 846 GHz in Faraday ( $\mathbf{k} \parallel \mathbf{H}$ ) and Voigt ( $\mathbf{k} \perp \mathbf{H}$ ) configuration for  $\mathbf{H} \parallel [100]$ ,  $\mathbf{H} \parallel [110]$ , and  $\mathbf{H} \parallel [001]$ . Vertical dotted lines, from left to right, indicate two-magnon resonance signal, signal of ESR standard DPPH, and one-magnon resonance signal, respectively.

estimates range from  $\Lambda/J \approx 8$  [15] to  $\Lambda/J = 5.8$  [22]. The associated spin shortening is  $\langle S \rangle \approx 1.3$  to 1.35, about 10% of the full spin value of  $3/2$  — in the magnetization curve, the magnetization at the saturation field is about 10% smaller from the fully saturated value in very high magnetic field. In comparison, the spin shortening in  $\text{Ba}_2\text{CoGe}_2\text{O}_7$  is  $\langle S \rangle = 1.491$ , less than 1%. This is why the magnetization curve shown in Fig. 2(a) is so flat above 18 T.

The far-infrared absorption spectra of the  $\text{Ba}_2\text{CoGe}_2\text{O}_7$  were studied in Ref. [22]. In comparison, the modes above the saturation field have a finite curvature — the signature of the stronger anisotropy. The multiboson spin-wave described the  $\text{Ba}_2\text{CoGe}_2\text{O}_7$  excitation spectrum with  $\Lambda = 13.4$  K,  $J = 2.3$  K,  $J_z = 1.8$  K — the values of the exchange coupling are very similar, it is the single-ion anisotropy that is different in the two materials.

## VI. SELECTION RULES

To further characterize the high field excitations, we compared the ESR spectra for the six geometries in Fig. 10. It appears that all the modes are active in the Voigt configurations. The only information about the matrix elements is provided by absence of the light absorptions in Faraday configurations. For example, in Fig. 10 the  $D_1$  is not present for the  $\mathbf{H} \parallel [100]$  case, and

the  $Q_1$  signal is missing when the external field is along the  $[110]$  and  $[001]$  directions. Since in the Faraday configuration the oscillating electric and magnetic fields of the incoming light are perpendicular to the direction of the external field, the missing absorption indicates that it is not excited by these components. In other words, it has no matrix elements with the perpendicular components of spin and polarization operators. Therefore, a signal present in Voigt, but absent in Faraday configuration, must be excited via the oscillating magnetic and/or electric fields which are parallel to the external field, and thus to the magnetic moments above saturation.

### A. Selection rules observed in the experiment

The situation discussed above happens in the case  $\mathbf{H} \parallel [100]$ , as the  $D_1$  magnon (open triangle in Fig. 10) is missing in the Faraday (dark green), but is present for the Voigt (light green) configuration. This means that only the  $[100]$  component of the light,  $H_{[100]}^\omega$  or  $E_{[100]}^\omega$  excites  $D_1$ . The  $Q_1$  bimagnon excitation (solid triangle in Fig. 10) is, however, present both in the Faraday and Voigt configuration, therefore it is coupled to the perpendicular  $[010]$  and/or  $[001]$  components.

Similarly, when  $\mathbf{H} \parallel [110]$ , the  $[\bar{1}10]$  and/or  $[001]$  components of the oscillating fields excite the  $D_1$  magnon present in Faraday and Voigt configurations, and the  $[110]$  parallel components create the  $Q_1$  bimagnon missing in the Faraday configuration but observed in the Voigt spectrum. Since we used unpolarized light, we cannot tell whether the  $E_{[110]}^\omega$  or/and  $H_{[110]}^\omega$  excite the  $D_1$  magnon mode from the experiment.

Finally, when  $\mathbf{H} \parallel [001]$ , it is the  $Q_1$  mode which appears in the Voigt configuration only, therefore it must be created by the parallel components  $H_{[001]}^\omega$  and/or  $E_{[001]}^\omega$ , and only by those components.

### B. Calculation of the selection rules above saturation from the magnetoelectric coupling

The magnetic component of the light can induce dipolar transitions only. It is the oscillating electric component of the light, coupled to polarization containing higher order spin-quadrupole operators, which can create the bimagnons. To verify this theory, we need to analyze the selection rules in different geometries in detail.

Above saturation, all the spins are parallel to the external field, making a translationally invariant ground state with  $\mathbf{q} = (0, 0)$ . The spin operator component parallel to the field  $S^\parallel$  does not change the number of magnons. The transversal fluctuations created by the perpendicular components  $S^{\perp 1}$  and  $S^{\perp 2}$  excite one magnon each. The two-magnon modes are created by the second order combinations of the perpendicular components. Furthermore, the polarization operators introduced in Eqs. (2)

are the sum of the uniform,  $\mathbf{q} = (0, 0)$ , and the staggered,  $\mathbf{q} = (\pi, \pi)$  components in the extended Brillouin zone, which can help further to classify excitations. The  $\mathbf{q} = (0, 0)$  components of the polarizations correspond to the terms proportional to  $\cos 2\kappa$ , and the  $\mathbf{q} = (\pi, \pi)$  components are proportional to  $\sin 2\kappa$  in Eqs. (2). Below we examine the selection rules for the different directions of the external magnetic field.

### 1. The case of $\mathbf{H} \parallel [001]$

This is the simplest case, as the parallel spin component is  $S^z$ , and the perpendicular components  $S^{\perp 1}$  and  $S^{\perp 2}$  correspond to  $S^x$  and  $S^y$ . From Eqs. (2) it is clear that only  $P^z$  contains second order terms in  $S^x$  and  $S^y$  – the  $\hat{Q}^{2xy}$  and  $\hat{Q}^{x^2-y^2}$ , therefore  $P_{\mathbf{q}}^z$  excites a bimagnon, both in the uniform  $\mathbf{q} = (0, 0)$  and in staggered  $\mathbf{q} = (\pi, \pi)$  channels, which we denoted by  $Q_0$  and  $Q_1$ .

From Eqs. (2) it is apparent that the perpendicular components,  $P_{\mathbf{q}}^x$  and  $P_{\mathbf{q}}^y$  are linear in  $S^x$  and  $S^y$  for both  $\mathbf{q} = (0, 0)$  and  $\mathbf{q} = (\pi, \pi)$ , therefore they can create electrically active magnetic modes. We label these dipolar excitations as  $D_0$  and  $D_1$ , depending whether they are active for the uniform or staggered polarizations. The electric selection rules for  $\mathbf{H} \parallel [001]$  are collected in the first row of Tab. I.

### 2. The case of $\mathbf{H} \parallel [110]$

The uniform polarization is the largest when the magnetic field is aligned with the  $[110]$  crystallographic direction, *i.e.* the  $x$ -axis. Then, the parallel spin component is  $S^x$  and the perpendicular ones are  $S^y$  and  $S^z$ . Observing Eqs. (2), we see that  $\hat{Q}^{2yz}$  appears in  $P_{(\pi, \pi)}^x$  and  $P_{(0, 0)}^y$ , and  $(S^y)^2$  is present in  $P_{(0, 0)}^z$ , so the quadrupolar  $Q_0$  mode can be excited via the perpendicular components of the uniform polarization operator  $P_{(0, 0)}^y$  and  $P_{(0, 0)}^z$ , and the  $Q_1$  mode is active for the staggered parallel component  $P_{(\pi, \pi)}^x$ . To determine the selection rules for the dipolar transitions, we need to find the components of the polarization operator which are linear in  $S^y$  and  $S^z$ . We get that the  $D_0$  dipolar mode is active for the uniform parallel component  $P_{(0, 0)}^x$ , while  $D_1$  can be excited via the staggered perpendicular components  $P_{(\pi, \pi)}^y$  and  $P_{(\pi, \pi)}^z$ , as summarized in the second row of Tab. I.

### 3. The case of $\mathbf{H} \parallel [100]$

When the field is set between the  $x$  and  $y$  axes, along the  $[100]$  direction, we choose the parallel and perpendic-

$\mathbf{H}$	$P_{(0,0)}^{\parallel}$	$P_{(\pi,\pi)}^{\parallel}$	$\perp$ -directions	$P_{(0,0)}^{\perp}$	$P_{(\pi,\pi)}^{\perp}$
$H \parallel [001]$	$(Q_0)$	$Q_1$	$[100]$ and $[010]$	$D_0$	$D_1$
$H \parallel [110]$	$D_0$	$Q_1$	$[\bar{1}10]$ and $[001]$	$(Q_0)$	$D_1$
$H \parallel [100]$	$(Q_0)$	$D_1$	$[010]$ and $[001]$	$D_0$	$Q_1$

TABLE I. The branches in the ESR spectrum the uniform  $P_{(0,0)}$  and staggered  $P_{(\pi,\pi)}$  components of the polarization excite. The electric field which couples to  $P^{\parallel}$  is present in Voigt configuration only, while the perpendicular components  $P^{\perp}$  are also present in Faraday configuration. The  $Q_0$  quadrupolar excitations are silent in the experiment.

ular components the spin operators as

$$\left( S_j^{\parallel}, S_j^{\perp 1}, S_j^{\perp 2} \right) = \left( \frac{S_j^x - S_j^y}{\sqrt{2}}, \frac{S_j^x + S_j^y}{\sqrt{2}}, S_j^z \right), \quad (28)$$

and analogous expression for the polarization. Thus, the parallel component of the polarization operator becomes

$$P_{(0,0)}^{\parallel} \propto \sum_j \hat{Q}_j^{2\perp 1 \perp 2} \quad \text{and} \quad P_{(\pi,\pi)}^{\parallel} \propto \sum_j (-1)^j \hat{Q}_j^{2\parallel \perp 2},$$

which can create a  $Q_0$  and a  $D_1$  excitation (last row of Tab. I), respectively. We choose  $[010]$  as the  $\perp_1$ , the polarizations are

$$P_{(0,0)}^{\perp 1} \propto \sum_j \hat{Q}_j^{2\parallel \perp 2} \quad \text{and} \quad P_{(\pi,\pi)}^{\perp 1} \propto \sum_j (-1)^j \hat{Q}_j^{2\perp 1 \perp 2},$$

and they couple to the  $D_0$  and  $Q_1$  modes. The other perpendicular direction is  $[001]$ , so  $P_{\mathbf{q}}^{\perp 2} = P_{\mathbf{q}}^z$  and

$$P_{(0,0)}^{\perp 2} \propto \sum_j \hat{Q}_j^{2\parallel \perp 1} \quad \text{and} \quad P_{(\pi,\pi)}^{\perp 2} \propto \sum_j (-1)^j \hat{Q}_j^{\perp 1 \perp 2}.$$

They excite  $D_0$  and  $Q_1$ , just like the  $P^{\perp 1}$ .

## C. Comparing to the experiment

Table I contains the central result of our paper: the experimental observations and theoretical calculation based on the magnetoelectric coupling are fully consistent with each other. Indeed, when  $\mathbf{H} \parallel [110]$  and the spins point along the  $x$  direction ( $S^{\parallel} \equiv S^x$ ), the staggered component of the  $\hat{P}_j^z$  creates a  $(\pi, \pi)$  magnon, giving rise to the  $D_1$  branch in Fig. 4. For  $\mathbf{H} \parallel [100]$ , the spin quadrupole operator in the staggered component of  $\hat{P}_j^z$  creates an  $S^{\parallel} = -1/2$  state with  $\mathbf{q} = (\pi, \pi)$  and energy Eq. (21d) leading to the  $Q_1$  resonance mode, in full agreement with the matrix elements shown in Table I.

Let us also mention that the  $D_1$  magnon mode is usually not observed in the ESR spectra, unless Dzyaloshinskii-Moriya interaction is present [35]. In

SCGO, however, it is the staggered component of the polarization can interact with the electric field of the light, leading to absorption at  $\mathbf{q} = (\pi, \pi)$ .

We also found above that the uniform component of the parallel polarizations can create quadrupole excitations at  $\mathbf{q} = (0, 0)$  as well, which we denoted as  $\mathbf{Q}_0$ . However, this mode is not seen in the experiment. The resolution of this puzzle lies in the structure of the two-magnon excitation spectrum. Two  $S^{\parallel} = 1/2$  magnons give rise to a two-magnon continuum, which is the broadest at  $\mathbf{q} = (0, 0)$ , extending from  $2\omega_{\mathbf{D}_1}$  to  $2\omega_{\mathbf{D}_0}$ . The on-site energy of the  $| -1/2 \rangle$  state is deep inside the continuum at  $\mathbf{q} = (0, 0)$ , and due to interactions with two  $S^{\parallel} = 1/2$  magnons it decays very quickly, making it unobservable. Only for very large anisotropy ( $\Lambda/J \gtrsim 7.5$ ) does the quadrupolar mode split off from the continuum for  $\mathbf{q} = (0, 0)$ . This is in sharp contrast with the case for the  $\mathbf{Q}_1$ , as the continuum shrinks to a single point at  $\mathbf{q} = (\pi, \pi)$  with energy  $\omega_{\mathbf{D}_0} + \omega_{\mathbf{D}_1} \neq \omega_{\mathbf{Q}_1}$ . In addition, the  $S^{\parallel} = -1/2$  state at  $\mathbf{q} = (\pi, \pi)$  is fully decoupled from the two-magnon continuum [29], resulting in a sharp absorption peak at  $\omega_{\mathbf{Q}_1}$ .

Although multipole fluctuations have long been theoretically proposed [36–39], the  $\mathbf{Q}_1$  mode in the saturated state of SCGO is, up to our knowledge, the first unambiguous experimental observation of a purely quadrupole excitation in a quantum magnet.

## VII. CONCLUSION

In conclusion, we studied multipole excitations in single crystals of the magnetoelectric insulator, SCGO. The observation of bimagnons is not new, they have been first observed in  $\text{FeI}_2$  [40], in the spin-1 chain compound,  $\text{NiCl}_2\text{-4SC}(\text{NH}_2)_2$  [41], as well as in the excitation spectrum of the other  $\ddot{\text{a}}\text{kermanites}$  [22] and even in ultracold atomic systems [42]. However, in those materials the single-ion anisotropy is the dominant term, reducing the spin length considerably and mixing the dipolar and quadrupolar degrees of freedom. As a result, magnon and bimagnon modes have both dipolar and quadrupolar character, and couple to magnetic and electric components of the exciting light in earlier experiments.

The nearly isotropic property of SCGO, on the other hand, allows for the emergence of uniquely pure quadrupolar excitations, appearing completely detached from magnetic transitions. Using multifrequency ESR technique, supported by theoretical investigation of transition matrix elements, we clarified the quadrupolar nature of the bimagnon excitation. Furthermore, based on analytical description of the excitations, available in the high field regime, and utilizing the measured saturation fields, we extracted the magnetic coupling values, as well as the components of the  $g$ -tensor with high precision. The spin wave spectra with the extracted parameter values are in excellent agreement with the measurements, throughout the entire magnetic field regime and for each

field direction.

Our investigations can serve as basis for further studies of emerging multipolar excitations with the use of well-spread experimental approaches, such as the ESR in the present work. Detecting such modes could help designing new magnetoelectric devices, in which electrically active magnetic excitations may carry and store information.

Furthermore, it may serve as a guide in the quest for nematic and more exotic, otherwise ‘hidden’ orders. By observing static properties such phases are usually experimentally undetectable due to the lack of magnetic ordering. An alternative route to reveal nematic phases is probing the dynamical properties and looking for the signatures of condensation of quadrupolar excitations at high magnetic fields, a prerequisite for the formation of spin nematic phase [30, 43–45]. For example, in  $\text{LiCuVO}_4$ , a high field phase just below the saturation is believed to be a spin nematic phase [46]. The NMR spin relaxation measurements showed a decay coming from excitations with twice as large slope as conventional magnons above the saturation field, indirectly supporting the condensation of such nematic waves [47]. The non-magnetic nature of those excitation was recently shown by another NMR experiment [48], however without explicitly proving the breaking of the  $O(2)$  symmetry, a defining property of the nematic state.

## ACKNOWLEDGMENTS

We thank K. Yamauchi, T. Oguchi, and M. Zhitomirsky for helpful discussions. This work was supported in part by the Grants-in-Aid for Scientific Research (Grant Nos. JP15K05145, JP25220803, JP24244059, and JP25246006) from MEXT, Japan and by JSPS Core-to-Core Program, A Advanced Research Networks and by the Hungarian OTKA Grant No. K106047. K.P. gratefully acknowledges support from the International Joint Research Promotion Program (Short Stay) of the Osaka University.

### Appendix A: The multiboson spin wave

In the next part we outline a simplified multiboson approach, in which we take a small single-ion anisotropy ( $\Lambda$ ) limit. By comparing our analytical solution to the measured spectrum we further prove the isotropic nature of this material.

#### 1. Variational setup

Here we will consider the Hamiltonian (7) assuming  $J_{pz} = 0$  for simplicity. We closely follow the derivation presented in Ref. [33]. Based on numerical calculations we need two variational parameters to characterize the ground state wave function, and consequently the bosons

representing the excited states, for all values of magnetic field.

We rotate the usual  $|m^z\rangle$  basis, with  $m^z = \langle S^z \rangle = -\frac{3}{2}, \dots, \frac{3}{2}$ , to a new basis, in which one of the states corresponds to the ground state. We perform such rotation on both sub-lattices in the following way

$$|\psi_0\rangle_A = \frac{|\frac{3}{2}\rangle - i\sqrt{3}\eta|\frac{1}{2}\rangle - \sqrt{3}\eta|\frac{-1}{2}\rangle + i|\frac{-3}{2}\rangle}{\sqrt{6\eta^2+2}}, \quad (\text{A1a})$$

$$|\psi_1\rangle_A = \frac{-i\sqrt{3}\eta|\frac{3}{2}\rangle - (2\eta-1)|\frac{1}{2}\rangle - i(2\eta-1)|\frac{-1}{2}\rangle - \sqrt{3}\eta|\frac{-3}{2}\rangle}{\sqrt{14\eta^2-8\eta+2}}, \quad (\text{A1b})$$

$$|\psi_2\rangle_A = \frac{-\sqrt{3}\eta|\frac{3}{2}\rangle - i|\frac{1}{2}\rangle - |\frac{-1}{2}\rangle - i\sqrt{3}\eta|\frac{-3}{2}\rangle}{\sqrt{6\eta^2+2}}, \quad (\text{A1c})$$

$$|\psi_3\rangle_A = \frac{i(2\eta-1)|\frac{3}{2}\rangle - \sqrt{3}\eta|\frac{1}{2}\rangle - i\sqrt{3}\eta|\frac{-1}{2}\rangle + (2\eta-1)|\frac{-3}{2}\rangle}{\sqrt{14\eta^2-8\eta+2}}, \quad (\text{A1d})$$

The transformation on sub-lattice  $B$  corresponds to the complex conjugate of Eqs. (A1). For  $\eta = 1$  these states represent the  $m^y = \frac{3}{2}, \dots, \frac{3}{2}$  basis, with  $|\psi_0\rangle_A = |m^y\rangle = -\frac{3}{2}$  and  $|\psi_0\rangle_B = |m^y\rangle = \frac{3}{2}$ . In other words, we changed the quantization axis to  $y$ . The value of  $\eta$  affects the length of the spin, which can be expressed as  $S = \frac{3\eta(1+\eta)}{1+3\eta^2}$ . In fact, below the saturation, due to the single-ion anisotropy term,  $\eta$  differs from 1 the spin length is shorter than  $\frac{3}{2}$ .

We consider two cases, when the field is in the  $xy$ -plane and when it is perpendicular to it. In the first case we set the field along the  $x$ -axis, that is along the [110] crystallographic direction. As long as no  $(P_i^z \cdot P_j^z)$  terms are considered, all in-plane directions are equivalent, and the spectrum looks the same –as far as the energy levels are concerned– for the directions [110] and [100].

To include the effect of magnetic field on the ground state, we need to allow the spins to turn away from the  $y$  axis, towards the direction of magnetic field.

In case of  $H\parallel[110]$ , therefore, we apply an additional rotation about the  $z$ -axis with the angles  $\pm\vartheta$  on sub-lattice  $A/B$ . The full variational setup for  $H\parallel[110]$  then has the form of  $|\Psi_i\rangle_A = e^{-i\vartheta S^z} |\psi_i\rangle_A$ , and  $|\Psi_i\rangle_B = e^{i\vartheta S^z} |\psi_i\rangle_B$ , ( $i = 0, \dots, 3$ ).

For perpendicular field,  $H\parallel[001]$ , we need a rotation about the  $x$ -axis with the angles  $\mp\vartheta$  on sub-lattice  $A/B$ . The variational setup for  $H\parallel[001]$  becomes  $|\Psi_i\rangle_A = e^{i\vartheta S^x} |\psi_i\rangle_A$ , and  $|\Psi_i\rangle_B = e^{-i\vartheta S^x} |\psi_i\rangle_B$ , ( $i = 0, \dots, 3$ ).

For both field directions the angle  $\vartheta$  changes from 0 to  $\pi/2$  as the spins tilt from the original  $y$ -axes towards the corresponding field direction. Evidently, when the spins are saturated along the  $x(z)$  direction  $\eta$  becomes 1 and  $\vartheta = \pi/2$ . In these simple cases, the new basis corresponds to the states  $\langle S^{x(z)} \rangle = -\frac{3}{2}, \dots, \frac{3}{2}$  on both sub-lattices, the ground state becomes  $\prod_{u.c.} |\Psi_0\rangle_A |\Psi_0\rangle_B = \prod_{u.c.} |m^{x(z)} = \frac{3}{2}\rangle_A |m^{x(z)} = \frac{3}{2}\rangle_B$ , and creating a state  $|\Psi_n\rangle$  with  $n = 1, 2$  or 3 on any of the sub-lattices corresponds to a transition of  $\Delta S^{x(z)} = n = 1, 2$  or 3, therefore, a dipolar, quadrupolar or octupolar transition.

We determine the variational parameters  $\eta$  and  $\vartheta$  by minimizing the ground state energy  $\langle \text{GS} | \mathcal{H} | \text{GS} \rangle$  with  $|\text{GS}\rangle = \prod_{u.c.} |\Psi_0\rangle_A |\Psi_0\rangle_B$ .

## 2. Static properties

To determine the magnetization and induced polarization as a function of external magnetic field, we calculate the expectation values of the spin and polarization operators **2** in the ground state. For in-plane magnetic field, the ground state is  $|\Psi_0\rangle_A = e^{-i\vartheta S^z} |\psi_0\rangle_A$ , and  $|\Psi_0\rangle_B = e^{i\vartheta S^z} |\psi_0\rangle_B$  only  $P^z$  is finite, and takes the value:

$$P^z = \frac{6\eta \cos(2(\kappa - \varphi))}{1 + 3\eta^2}. \quad (\text{A2})$$

Substituting the values for the variational parameters  $\eta$  from Eq. A5 and  $\vartheta$  from Eq. A4 we plotted the theoretical induced polarization. Of course, including the polarization–polarization term would give a better agreement with the experimentally measured polarization and would reproduce the drop of  $P^z$  to zero at small field. [17]

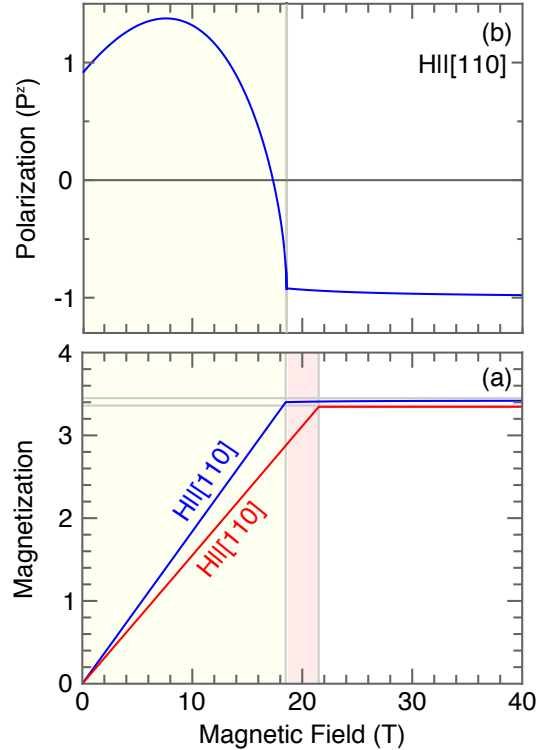


FIG. 11. (a) Calculated magnetization using our variational setup using the variational parameters determined below in Sec. A3 and Sec. A4 for in-plane and out-of-plane magnetic fields, respectively. (b) Theoretically calculated induced polarization in the simplified picture using Eq. A2. We neglected the polarization–polarization term in the Hamiltonian, and use the small  $\Lambda$  expansion. If  $P_i^z \cdot P_j^z$  were kept, the polarization would drop to zero at zero field. For both figures we used the  $g$  and interaction values from the linear fit in Eqs. 25 and 26 in the main text.

### 3. In-plane magnetic field

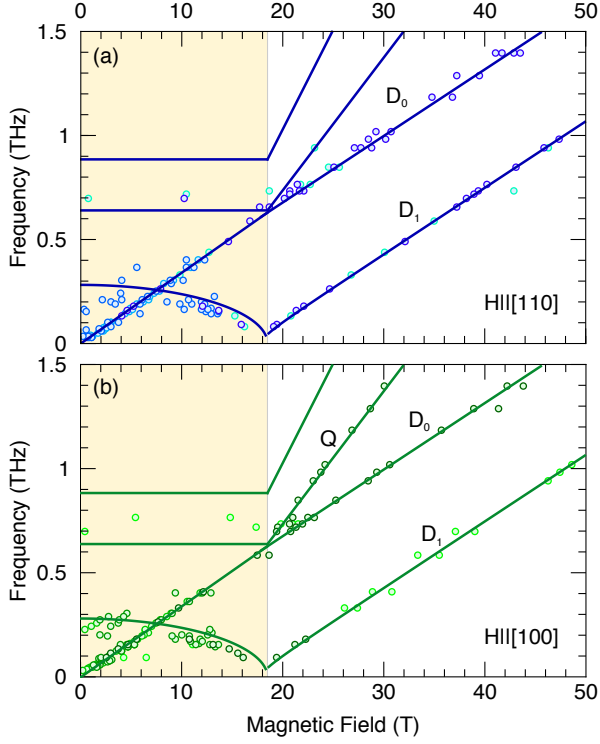


FIG. 12. Simplified multiboson approach compared with the measured ESR spectrum for field directions parallel to the  $H||[110]$  and  $H||[100]$  crystallographic direction in (a) and (b), respectively. The energy of dipole and quadrupole excitation is in very good agreement with the experimental findings.

For fields lying in the  $xy$ -plane the ground state energy has the following form

$$E_0 = -36J \cos 2\vartheta \frac{(1+\eta)^2 \eta^2}{(1+3\eta^2)^2} - 6g_{ab}H^x \sin \vartheta \frac{\eta(1+\eta)}{1+3\eta^2} + \Lambda \frac{3(3+\eta^2)}{2(1+3\eta^2)}. \quad (\text{A3})$$

Although this can be minimized analytically, we restrict ourselves to the limit, in which  $\Lambda$  is a small parameter. The variational parameters take the following

form:

$$\vartheta = \begin{cases} \arcsin \frac{g_{ab}H^x}{12J}, & g_{ab}H^x < 12J \\ \pi/2, & g_{ab}H^x \geq 12J \end{cases} \quad (\text{A4})$$

and

$$\eta = \begin{cases} 1 + \frac{\Lambda}{6J}, & g_{ab}H^x < 12J \\ 1 + \frac{\Lambda}{g_{ab}H^x - 6J}, & g_{ab}H^x \geq 12J \end{cases} \quad (\text{A5})$$

At zero field the spins are antiparallel along the  $y$ -axis. In finite field the spins start to tilt towards each-other to align themselves with the field direction.  $H_c^x = 12J/g_{ab}$  gives the transition field, at which the spins become parallel to each-other and  $H^x$  as well. Above  $H_c^x$  their length grows asymptotically approaching the maximal  $3/2$  value.

Taking the small  $\Lambda$  limit, we can continue our analysis with the excitation spectrum, in which the different multipole excitations decouple from each-other and we get simple equations of motion describing them separately.

As the next step, we express each operator in the Hamiltonian 7 in terms of our new basis, using the transformation  $\hat{U} = (\Psi_0, \Psi_1, \Psi_2, \Psi_3)$ . in which the columns correspond to the component vectors of the new states  $|\Psi_i\rangle$ ,  $i = 0, \dots, 3$ .

We introduce a boson for each of the states  $a_{i,L}^\dagger |0\rangle = |\Psi_i\rangle_L$ , where  $i = 0, \dots, 3$  and  $L = \{A, B\}$ . The mean-field ground state is the product state  $\prod_{u.c.} |\Psi_0\rangle_A |\Psi_0\rangle_B$  in which the boson  $a_{0,L}^\dagger$  is condensed on both sub-lattices. Creating a boson  $a_{n,L}^\dagger$  with  $n = 1, 2$  or  $3$  corresponds to an excitation with dipole, quadrupole or octupole character, respectively.

Let us start with the dipole excitation. The spin-wave Hamiltonian for these modes has the form

$$\mathcal{H}_D = \begin{pmatrix} a_{1,A}^\dagger \\ a_{1,B}^\dagger \\ a_{1,A} \\ a_{1,B} \end{pmatrix}^T \begin{pmatrix} \varepsilon_0 & f_+ & 0 & f_- \\ f_+ & \varepsilon_0 & f_- & 0 \\ 0 & f_- & \varepsilon_0 & f_+ \\ f_- & 0 & f_+ & \varepsilon_0 \end{pmatrix} \begin{pmatrix} a_{1,A} \\ a_{1,B} \\ a_{1,A}^\dagger \\ a_{1,B}^\dagger \end{pmatrix}, \quad (\text{A6})$$

where  $\varepsilon_0 = 6J \cos 2\vartheta + g_{ab}H_x \sin \vartheta + \Lambda$  and  $f_\pm = 3J\eta \cos(2\vartheta) \pm 3J_z(\eta - 2)$ . Inserting the solutions Eqs. A4 and A5 we get

$$\omega_{D_0} = \begin{cases} g_{ab}H^x \sqrt{1 + \frac{\Lambda}{6J}} \sqrt{1 + \frac{J_z - J}{2J} \left(1 - \frac{\Lambda}{6J}\right)}, & g_{ab}H^x < 12J \\ g_{ab}H^x - 3J + 3J_z + \Lambda \left( \frac{J+J_z}{2J_z} - \frac{3(J-J_z)}{g_{ab}H^x} \right), & g_{ab}H^x \geq 12J \end{cases} \quad (\text{A7})$$

and

$$\omega_{D_1} = \begin{cases} (6J + \Lambda) \sqrt{2 \left(1 - \left(\frac{g_{ab}H^x}{12J}\right)^2\right) \left(1 + \frac{J_z}{J} - \frac{12J_z}{6J + \Lambda}\right)}, & g_{ab}H^x < 12J \\ g_{ab}H^x - 9J - 3J_z + \Lambda \left(1 - \frac{(J - J_z)(g_{ab}H^x - 6J_z)}{2J_z(g_{ab}H^x - 12J_z)}\right)}, & g_{ab}H^x \geq 12J \end{cases} \quad (\text{A8})$$

The quadrupolar and octupolar modes are even more straightforward, as the Hamiltonian describing their dynamics is diagonal and we can directly read off the energies.

The two quadrupole modes,  $a_{2,A}^\dagger$  and  $a_{2,B}^\dagger$ , are degenerate and have the energies

$$\omega_Q = 12J \cos 2\vartheta + 2g_{ab}H_x \sin \vartheta + \frac{\Lambda}{2}(3\eta - 1) \quad (\text{A9})$$

Substituting the solutions Eqs. A4 and A5 we get

$$\omega_Q = \begin{cases} 12J + \Lambda, & g_{ab}H^x < 12J \\ 2g_{ab}H^x - 12J + \Lambda, & g_{ab}H^x \geq 12J \end{cases} \quad (\text{A10})$$

The octupole modes  $a_{3,A}^\dagger$  and  $a_{3,B}^\dagger$  are also degenerate with the energy

$$\omega_O = \begin{cases} 18J, & g_{ab}H^x < 12J \\ 3g_{ab}H^x - 18J, & g_{ab}H^x \geq 12J \end{cases} \quad (\text{A11})$$

In Fig. 12 we plot the measured spectrum and the analytical solutions A7, A8, A10 and A11 using the model parameters  $g_{ab} = 2.28$  and Eqs. 26 determined from experimental data as explained in the main text. We find an excellent agreement between our simple model and the experiment, further justifying our assumption for the large field limit and the determined parameters.

#### 4. Perpendicular field

For magnetic field applied perpendicular to the layers, the angle  $\vartheta$  measures the canting from the  $y$ -axis towards the  $z$ -axis and the ground state energy becomes

$$\begin{aligned} E_0 = & -36 \frac{(1 + \eta)^2 \eta^2}{(1 + 3\eta^2)^2} (J \cos^2 \vartheta - J_z \sin^2 \vartheta) \\ & + \Lambda \frac{3(3 + \eta^2)}{2(1 + 3\eta^2)} + \Lambda \frac{3(1 + \eta)(3\eta - 1)}{(1 + 3\eta^2)} \sin^2 \vartheta \\ & - 6g_z H^z \sin \vartheta \frac{\eta(1 + \eta)}{1 + 3\eta^2}. \end{aligned} \quad (\text{A12})$$

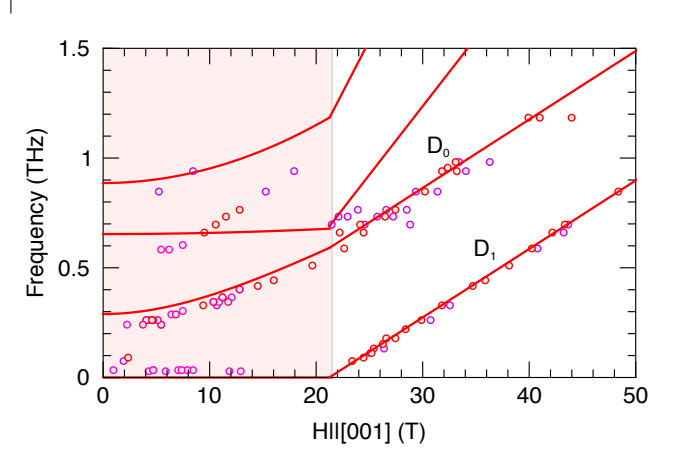


FIG. 13. Simplified multiboson approach compared with the measured spectrum for field parallel to the  $H||[001]$  crystallographic direction.

We again look for the solution up to leading order in  $\Lambda$ , and obtain

$$\vartheta = \begin{cases} \arcsin \delta, & \delta < 1 \\ \pi/2, & \delta \geq 1 \end{cases} \quad (\text{A13})$$

where we introduced the parameter  $\delta = \frac{g_z H^z}{6J + 6J_z + 2\Lambda}$  which gives the transition field upon becoming unity. For  $\delta = 1$  the magnetic field reaches the value  $H^z = \frac{6J + 6J_z + 2\Lambda}{g_z}$  at which the spins become parallel to each other as well as the magnetic field.

$$\eta = \begin{cases} 1 + \frac{\Lambda}{6J}(1 - \delta^2), & \delta < 1 \\ 1, & \delta \geq 1 \end{cases} \quad (\text{A14})$$

The spin-wave Hamiltonian describing the dynamics of dipole excitations can be written in the same form as Eq. A6 with the parameters  $\varepsilon_0 = -6J_z + 6(J + J_z) \cos^2 \vartheta + \frac{\Lambda}{2}(3 \cos(2\vartheta) - 1) + g_c H^z \sin \vartheta$ ,  $f_{\pm} = 3J\eta \pm 3(J - J_z)(1 - \frac{\eta}{2}) \mp 3(J + J_z) \cos(2\vartheta)(1 - \frac{\eta}{2})$ .

The energies of the dipolar excitations can be easily calculated using Eqs. A13- A14.

$$\omega_{D_1} = \begin{cases} 0, & \delta < 1 \\ -6J - 6J_z + g_c H^z - 2\Lambda, & \delta \geq 1 \end{cases} \quad (\text{A15})$$

and

$$\omega_{D_0} = \begin{cases} \sqrt{6J + \Lambda(1 - \delta^2)} \sqrt{24J - 12(J + J_z)(1 - \delta^2)(1 - \frac{\Lambda(1 - \delta^2)}{6J})}, & \delta < 1 \\ 6J - 6J_z + g_c H^z - 2\Lambda, & \delta \geq 1 \end{cases} \quad (\text{A16})$$

where  $\eta$  is the solution below the transition field ( $\delta < 1$ ).

The spin-wave Hamiltonian for quadrupole and octupole excitations become diagonal for  $H \parallel [001]$  too, and we can easily read off the eigenvalues. Similarly to the in-plane field case, the modes are two-fold degenerate.

$$\omega_Q = \begin{cases} 12J + \Lambda + \frac{\Lambda^2}{4J} + \Lambda\delta^2(1 - \frac{\Lambda}{2J}), & \delta < 1 \\ 2g_z H^z - 12J_z - 2\Lambda, & \delta \geq 1 \end{cases} \quad (\text{A17})$$

$$\omega_O = \begin{cases} 18J + \frac{\Lambda^2}{4J} + 6\Lambda\delta^2(1 - \frac{\Lambda}{12J}), & \delta < 1 \\ 3g_z H^z - 18J_z, & \delta \geq 1 \end{cases} \quad (\text{A18})$$

In Fig. 13 we plot the calculated energies together with the measured spectrum for  $H \parallel [001]$  and find excellent agreement between our simple model and the observed spectrum.

- 
- [1] M. Fiebig, J. Phys. D **38** R123 (2005).  
[2] Y. Tokura, S. Seki and N. Nagaosa, Rep. Prog. Phys. **77** 076501 (2014).  
[3] T. Arima, J. Phys. Soc. Jpn. **80** 052001 (2011).  
[4] T. Kimura, T. Goto, H. Shintani, K. Ishizaka, T. Arima, and Y. Tokura, Nature (London) **426**, 55 (2003).  
[5] H. Katsura, N. Nagaosa, and A. V. Balatsky, Phys. Rev. Lett. **95**, 057205 (2005).  
[6] I. A. Sergienko and E. Dagotto, Phys. Rev. B **73**, 094434 (2006).  
[7] C. Jia, S. Onoda, N. Nagaosa, and J. H. Han, Phys. Rev. B **76**, 144424 (2007).  
[8] M. Akaki, H. Iwamoto, T. Kihara, M. Tokunaga, and H. Kuwahara, Phys. Rev. B **86**, 060413(R) (2012).  
[9] T. Arima, J. Phys. Soc. Jpn. **76**, 073702 (2007).  
[10] H. Y. Yi, Y. J. Choi, S. Lee, and S.-W. Cheong, Appl. Phys. Lett. **92**, 212904 (2008).  
[11] H. Murakawa, Y. Onose, S. Miyahara, N. Furukawa, and Y. Tokura, Phys. Rev. Lett. **105**, 137202 (2010).  
[12] M. Akaki, J. Tozawa, D. Akahishi, and H. Kuwahara, Appl. Phys. Lett. **94**, 212904 (2009).  
[13] M. Akaki, H. Kuwahara, A. Matsuo, K. Kindo, and M. Tokunaga, J. Phys. Soc. Jpn. **83**, 093704 (2014).  
[14] I. Kézsmárki, N. Kida, H. Murakawa, S. Bordács, Y. Onose, and Y. Tokura, Phys. Phys. Lett. **106**, 057403 (2011).  
[15] S. Miyahara and N. Furukawa, J. Phys. Soc. Jpn. **80**, 073708 (2011).  
[16] I. Kézsmárki, D. Szaller, S. Bordács, V. Kocsis, Y. Tokunaga, Y. Taguchi, H. Murakawa, Y. Tokura, H. Engelkamp, T. Rõöm, and U. Nagel, Nature Communications **5**, 3203 (2014).  
[17] J. Romhányi, M. Lajkó, and K. Penc, Phys. Rev. B **84**, 224419 (2011).  
[18] M. Soda, M. Matsumoto, M. Månsson, S. Ohira-Kawamura, K. Nakajima, R. Shiina, and T. Masuda, Phys. Rev. Lett. **112** 127205 (2014).  
[19] T. Endo, Y. Doi, Y. Hinatsu, and K. Ohoyama, Inorg. Chem. **51**, 3572-3578 (2012).  
[20] A. Zheludev, T. Sato, T. Masuda, K. Uchinokura, G. Shirane, and B. Roessli Phys. Rev. B **68**, 024428 (2003).  
[21] V. Hutanu, A. P. Sazonov, M. Meven, G. Roth, A. Gukasov, H. Murakawa, Y. Tokura, D. Szaller, S. Bordács, I. Kézsmárki, V. K. Guduru, L. C. J. M. Peters, U. Zeitler, J. Romhányi, and B. Náfrádi, Phys. Rev. B **89**, 064403 (2014).  
[22] K. Penc, J. Romhányi, T. Rõöm, U. Nagel, Á. Antal, T. Fehér, A. Jánosy, H. Engelkamp, H. Murakawa, Y. Tokura, D. Szaller, S. Bordács, and I. Kézsmárki, Phys. Rev. Lett. **108**, 257203 (2012).  
[23] K. Yamauchi, P. Barone, and S. Picozzi, Phys. Rev. B **84**, 165137 (2011).  
[24] M. Matsumoto and M. Koga, J. Phys. Soc. Jpn. **76**, 073709 (2007).  
[25] T. Nagamiya, K. Yosida, and R. Kubo, Advances in Physics **4**, 1 (1955).  
[26] M. Wortis, Phys. Rev. **132**, 85 (1963),  
[27] J. Hanus, Phys. Rev. Lett. **11**, 336 (1963).  
[28] D. C. Mattis, The Theory of Magnetism I (Springer, Berlin) 1988.  
[29] R. Silberglitt and J. B. Torrance, Jr., Phys. Rev. B **2**, 772 (1970).  
[30] M. E. Zhitomirsky and H. Tsunetsugu, Europhysics Letters **92**, 37001 (2010).  
[31] See Supplemental Material at ... for a movie of the  $D_1$  and  $Q_1$  modes in the 3 different geometries. Green arrows represent the expectation values of the spin operators, the red arrows the spin-induced electric polarization, and blue arrow the direction of the external magnetic field. The uniform components are shown on the right side side of the movies, together with the coordinate system, and the modes active in the Faraday and Voigt geometries are easily identified. The spins are represented using the coherent state representation, see [45]  
[32] We use  $1 \text{ THz} = 48.0 \text{ K}$  and  $\mu_B = 0.6717 \text{ K T}^{-1} = 13.996 \text{ GHz T}^{-1}$  for unit conversion.  
[33] J. Romhányi and K. Penc, Phys. Rev. B **86**, 174428 (2012).

- [34] P. A. Lindgard and A. Kowalska, *Journal of Physics C: Solid State Physics* **11**, 2081 (1976); P. S. Riseborough, *Solid State Communications* **48**, 901 (1983).
- [35] S. A. Zvyagin, D. Kamenskyi, M. Ozerov, J. Wosnitza, M. Ikeda, T. Fujita, M. Hagiwara, A. I. Smirnov, T. A. Soldatov, A. Ya. Shapiro, J. Krzystek, R. Hu, H. Ryu, C. Petrovic, and M. E. Zhitomirsky, *Phys. Rev. Lett.* **112**, 077206 (2014).
- [36] A. V. Chubukov, *J. Phys.: Condens. Matter* **2** (1990).
- [37] F. P. Onufrieva, *Physica B* **186-188** 837-840 (1993).
- [38] R. Shiina, H. Shiba, P. Thalmeier, A. Takahashi and O. Sakai, *J. Phys. Soc. Jpn.* **72**, 1216 (2003).
- [39] M. Matsumoto, *J. Phys. Soc. Jpn.* **83**, 084704 (2014).
- [40] A.R. Fert, D. Bertrand, J. Leotin, J.C. Ousset, *Solid State Communications* **26**, 693 (1978); D. Petitgrand, A. Brun, P. Meyer, *Journal of Magnetism and Magnetic Materials* **15**, 381 (1980); K. Katsumata, H. Yamaguchi, M. Hagiwara, M. Tokunaga, H.-J. Mikeska, P. Goy, and M. Gross, *Phys. Rev. B* **61**, 11632 (2000).
- [41] S. A. Zvyagin, J. Wosnitza, C. D. Batista, M. Tsukamoto, N. Kawashima, J. Krzystek, V. S. Zapf, M. Jaime, N. F. Oliveira, Jr., and A. Paduan-Filho, *Phys. Rev. Lett.* **98**, 047205 (2007).
- [42] T. Fukuhara, P. Schauß, M. Endres, S. Hild, M. Cheneau, I. Bloch and C. Gross, *Nature* **502**, 76 (2013).
- [43] A. V. Chubukov, *Phys. Rev. B* **44**, 4693 (1991); N. Shannon, T. Momoi, and P. Sindzingre, *Phys. Rev. Lett.* **96**, 027213 (2006).
- [44] F. Heidrich-Meisner, A. Honecker, and T. Vekua, *Phys. Rev. B* **74**, 020403(R) (2006); T. Hikihara, L. Kecke, T. Momoi, and A. Furusaki, *Phys. Rev. B* **78**, 144404 (2008); J. Sudan, A. Lüscher, and A. M. Läuchli, *Phys. Rev. B* **80**, 140402(R) (2009).
- [45] A. M. Läuchli, F. Mila, and K. Penc, *Phys. Rev. Lett.* **97**, 087205 (2006).
- [46] L. E. Svistov, T. Fujita, H. Yamaguchi, S. Kimura, K. Omura, A. Prokofiev, A. I. Smirnov, Z. Honda, and M. Hagiwara, *JETP Lett.* **93**, 21 (2011).
- [47] N. Büttgen, K. Nawa, T. Fujita, M. Hagiwara, P. Kuhns, A. Prokofiev, A. P. Reyes, L. E. Svistov, K. Yoshimura, and M. Takigawa, *Phys. Rev. B* **90**, 134401 (2014).
- [48] A. Orlova, E. L. Green, J. M. Law, D. I. Gorbunov, G. Chanda, S. Kramer, M. Horvatic, R. K. Kremer, J. Wosnitza, and G. L. J. A. Rikken, *Phys. Rev. Lett.* **118**, 247201 (2017).